

IMECE2014-37682

DESIGN AND PROTOTYPING OF A COST-EFFECTIVE SUN TRACKING SYSTEM FOR PHOTOVOLTAIC PANELS

Adrian GEORGESCU

School of Engineering and Comp. Sciences,
Texas A&M University Corpus Christi
6300 Ocean Drive, Unit 5733,
Corpus Christi, TX 78412, USA
adrian.georgescu@tamucc.edu

P. A. SIMIONESCU

School of Engineering and Comp. Sciences,
Texas A&M University Corpus Christi
6300 Ocean Drive, Unit 5733,
Corpus Christi, TX 78412, USA
pa.simionescu@tamucc.edu
(corresponding author)

Ilie TĂLPĂȘANU

Department of Mechanical
Engineering and Technology,
Wentworth Institute of Technology,
Boston, MA 02115
talpasanui@wit.edu

ABSTRACT

The paper discusses the design and prototype build of a sun tracking system for photovoltaic panels, that consists of a slider-rocker mechanism and a controls system. The slider-rocker is optimized for best transmission angle properties, near linear input-output function and 180 degrees rocker travel. The control system includes three shaded light-dependent resistors pointing in different directions, and operational amplifiers to sense the imbalance in their illumination. The amplified imbalanced signal is used to control the linear motor of the slider-rocker mechanism towards minimizing this imbalance. A small scale prototype of the system has been built and tested successfully.

INTRODUCTION

From the early days of photovoltaic (PV) solar energy conversion, engineers have recognized the benefit of tracking the sun, versus maintaining the orientation of the PV panel stationary [1]. In flat-panel PV applications, solar trackers are employed to minimize the angle of incidence between the incoming sunlight, and thus increases the amount of energy produced. As the sun travels east to west about 180° during an average day (this travel is more in summer months than in the winter), a PV panel in a fixed orientation will capture less than 25% of the incident energy in the morning and evening [2]. In

addition, the sun also moves through 46° north and south during a year, and for a PV panel set at the midpoint between the summer and winter solstice extremes will experience additional energy losses of up to 8.3% [3]. Rotating the panels towards the sun can help recapture those losses. A tracker that rotates in the east-west direction only is known as a *single-axis sun tracker*. A tracker that accounts for both the daily and seasonal changes in solar incidence is called *dual-axis tracker*. High accuracy tracking is not typically required in PV applications. More important for practical applications are mechanical simplicity, low installation and maintenance costs, and resistance to wind-loading [3,4].

Compared to single axis trackers, dual-axis sun trackers are more complex and require more frequent maintenance, which are not always justified by their energy output gain. The majority of commercial sun trackers use slewing drives of the worm-wheel gear type [5]. Other designs use linear motors, or linkage amplifiers capable of synchronizing the motion of multiple PV panels using a single driving motor and a single control system [6]. References [7-10] describe various sun trackers designs, all of them being more complex than the one discussed in this paper.

Most solar tracking systems available today have a sweep angle limited to about 150°, mainly due to limitations imposed by the spacing between different panels. The design discussed

in this paper allows for a 180° azimuthal angle, thus being able to efficiently capture light in early-sunrise or late-sunset. According to [11], at those large angles, the solar irradiance can be approximated by the formula:

$$I = 1.1 \times I_0 \times 0.7^{AM^{0.678}} \quad (1)$$

where I is the solar irradiance, I_0 is the solar irradiance outside the atmosphere (both in W/m^2) and AM is the air mass. This translates into an irradiance of $270 W/m^2$ at incidence angles of $\pm 85^\circ$, which is more than a quarter of the power available in $AM=1.5$ conditions, considered standard. It is known that PV panels have their efficiency at lower temperatures increased by a coefficient of about $0.0045/^\circ C$ [11]. This makes systems that implement an azimuthal sweep angle close to 180° more advantageous, because of the lower ambient temperature in the morning and late afternoon hours.

This paper discusses the main elements of a prototype single-axis sun tracker (Figure 1), consisting of a photovoltaic panel mounted on a pivotal axle, slider-rocker actuator and electronic controls system.



Figure 1: Single-axis solar tracking PV panel prototype.

MECHANICAL ACTUATOR

The mechanical actuator of the azimuthal axis PV tracker is a slider-rocker mechanism as shown in Figure 2, of link lengths AB , OB and slider offset y_A . A rocker travel $\Delta\varphi = \varphi_1 - \varphi_0$ is imposed to be generated for a linear motor displacement s_{max} corresponding to joint A moving between points (x_{A0}, y_A) and (x_{A1}, y_A) .

For the correlated positions (x_{A0}, φ_0) and (x_{A1}, φ_1) of the input and output members, the synthesis equations of the linkage are:

$$\begin{aligned} AB^2 &= (x_{A0} - x_{B0})^2 + (y_{A0} - y_{B0})^2 \\ AB^2 &= (x_{A1} - x_{B1})^2 + (y_{A1} - y_{B1})^2 \end{aligned} \quad (2)$$

where:

$$\begin{aligned} x_{B0} &= OB \cdot \cos \varphi_0 & y_{B0} &= OB \cdot \sin \varphi_0 \\ x_{B1} &= OB \cdot \cos \varphi_1 & y_{B1} &= OB \cdot \sin \varphi_1 \end{aligned} \quad (3)$$

For $y_{A0} = y_{A1} = y_A$ equations (1) and (2) yield:

$$AB^2 = x_{A0}^2 - 2OB \cdot (x_{A0} \cos \varphi_0 + y_A \sin \varphi_0) + OB^2 + y_A^2 \quad (4)$$

$$AB^2 = x_{A1}^2 - 2OB \cdot (x_{A1} \cos \varphi_1 + y_A \sin \varphi_1) + OB^2 + y_A^2 \quad (5)$$

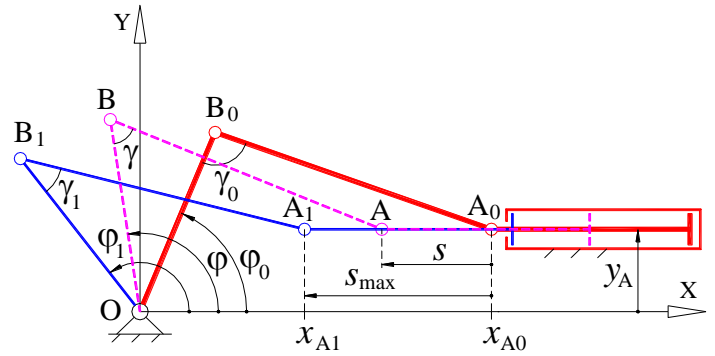


Figure 2: PRRR mechanism shown in its limit positions $(0, \varphi_0)$, (s_{max}, φ_1) and in an intermediate position (s, φ) .

Subtracting equation (4) from equation (5), and after substituting $x_{A1} = x_{A0} - s_{max}$ and $\varphi_1 = \varphi_0 + \Delta\varphi$, the length of the rocker is obtained i.e.

$$\begin{aligned} OB &= s_{max} (x_{A0} - 0.5s_{max}) / (x_{A0} \cos \varphi_0 - (x_{A0} - s_{max}) \cdot \\ &\cos(\varphi_0 + \Delta\varphi) + y_A (\sin \varphi_0 - \sin(\varphi_0 + \Delta\varphi))) \end{aligned} \quad (6)$$

Any parameters φ_0 , x_{A0} and y_A that satisfy equations (4) and (6) are potential solution to the requirement that the prescribed limit positions are obtained with the given actuator stroke s_{max} . These three parameters will be tuned in a numerical optimization process seeking that: (a) the transmission angle γ exhibits minimum departure from 90° over the entire working range of the mechanism, and (b) that a near linear correlation between input and output are satisfied.

For the piston joint A located at x_A , the transmission angle γ can be calculated with:

$$\gamma(x_A) = \arccos \left(\frac{OB^2 + AB^2 - x_A^2 - y_A^2}{2 \cdot OB \cdot AB} \right), \quad (7)$$

The maximum and minimum values of this angle occur for slider positions $x_A = x_{A0}$, $x_A = x_{A1}$ and (if it is within the working range of the mechanism) for $x_A = 0$.

In order to find the link-lengths of the mechanism that will generate a prescribed rocker travel $\Delta\phi$ while simultaneously satisfying a minimum departure from 90° of the transmission angle, the following *mini-max* problem in the design variables ϕ_0 , x_{A0} and y_A has been formulated:

$$\text{minimize } F(\phi_0, x_{A0}, y_A) = \max\{c_0, c_1, c_e\}$$

where

$$(8)$$

$$c_0 = |\cos \gamma(x_{A0})|$$

$$c_1 = |\cos \gamma(x_{A1})|$$

$$c_e = \begin{cases} |\cos \gamma(0)| & \text{if } x_{A0} \cdot x_{A1} < 0 \\ 0 & \text{if } x_{A0} \cdot x_{A1} \geq 0 \end{cases}$$

When minimizing the objective function in equation (8), it is essential to consider only those configurations for which the triangular loop O-A-B maintains the same orientation, or otherwise the two limit positions cannot be attained without breaking the joints. This was done by verifying that the cross products $\mathbf{OB}_0 \times \mathbf{B}_0\mathbf{A}_0$, $\mathbf{OB}_e \times \mathbf{B}_e\mathbf{A}_e$ and $\mathbf{OB}_1 \times \mathbf{B}_1\mathbf{A}_1$ (corresponding to the mechanism in its three critical positions) are all positive.

In order to ensure a near linear dependence between input and output, the following penalty function has been added to optimization problem (8):

$$\varepsilon = \text{Max}_{j=1}^n \left| s_j + \frac{\phi_0 - \phi(s_j)}{\Delta\phi} \right|$$

$$(9)$$

evaluated for a number of $n=30$ discrete positions s_j , corresponding to the actuator moving between 0 and s_{\max} . In the above equation (9), the term $\phi(s_j)$ is solution to the equation:

$$a \cos(\phi) + b \sin(\phi) = c$$

$$(10)$$

that is:

$$\phi = \text{Atan2}(b, a) \pm \text{Atan2}\left(\sqrt{a^2 + b^2 - c^2}, c\right)$$

$$(11)$$

where constants a , b and c are:

$$\begin{aligned} a &= 2OB \cdot x_A \\ b &= 2OB \cdot y_A \\ c &= OB^2 - AB^2 + x_A^2 + y_A^2. \end{aligned}$$

$$(12)$$

Equation (10) has been obtained by projecting vector loop equation $\mathbf{BO}-\mathbf{OA}=\mathbf{AB}$ of the mechanism on the X and Y axes of the fixed reference frame visible in Figure 2, and then squaring and adding the corresponding scalar components.

Objective function (8) with penalty (9) has been minimized for the case of maximum admissible linearity error $\varepsilon_{\text{adm}}=0.05$.

The optimum mechanism, obtained by performing a multi-start *Nadler-Mead* optimum search [12], has the following geometry: $x_{A0}=85.48$ mm, $y_A=30.78$ mm, $\phi=38.51^\circ$, $OB=38.06$ mm, $AB=56.16$ mm. Its transmission angle range is: $31.24^\circ \leq \gamma \leq 148.76^\circ$. A schematic of this mechanism, together with a plot of the displacement function $\phi(s)$ and transmission angle function $\gamma(s)$ are given in Figure 3. Also given in Figure 3 is a plot of the kinematic coefficient $d\phi/ds$ [13]. Knowing this coefficient allows one to calculate the input actuator force \mathbf{P} required to overcome an output resisting torque \mathbf{M} using the *Principle of Virtual Work* [14]:

$$\mathbf{P} \cdot ds = \mathbf{M} \cdot d\phi$$

$$(13)$$

Notice that there are two positions where the ratio $d\phi/ds$ is maximum, occurring for $s=s_{\max}$ and for $s=0.29 \cdot s_{\max}$ (see Figure 3, and also references [15] and [16] where the tools used to produce the graph and kinematic simulation are described). In these two positions, one Newton of linear motor force can hold 5.1 N-m and 4.15 N-m of resisting torque at the PV panel axis respectively. These positions can be designed as safe positions, where the solar tracker can be parked in the event of turbulent weather. Conversely, for $s=0$ the system is most sensitive to offset loading of the solar-panel.

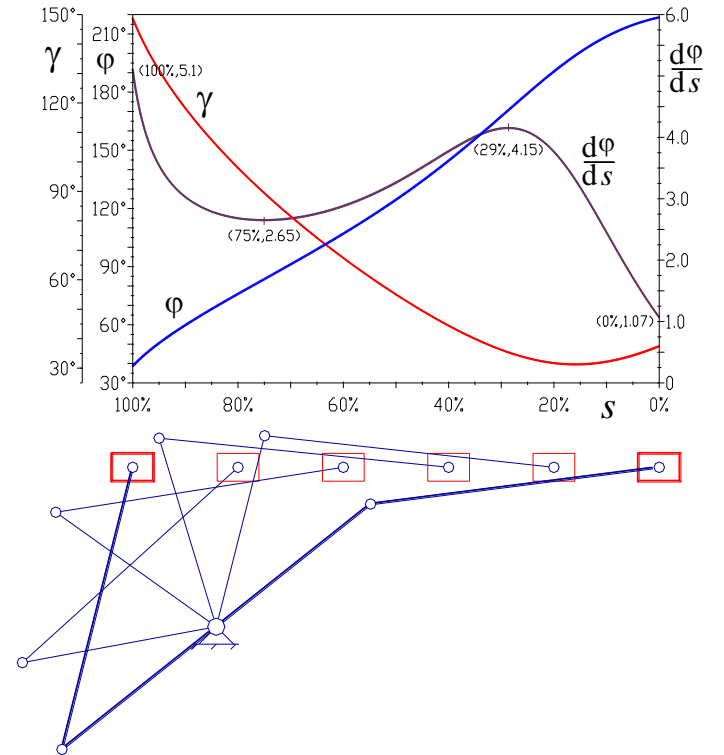


Figure 3: Performance plot and skeleton diagram of the optimized actuator mechanism, with the slider travel aligned with the horizontal axis of the plot.

ELECTRICAL CIRCUIT

In order to determine the relative position of the sun, three shaded *light dependent resistors* (LDR) are used, noted LDR1, LDR2 and LDR3 in Figure 4. Two of them are placed on the front of the solar panel, and one on the back (i.e. LDR2). The use of LDR2 will eliminate the ambiguity caused at sunrise, when the incident light will hit the panel from behind as it was left the evening before. To increase the system sensitivity, two small screens were placed in the vicinity of LDR1 and LDR3, so that even slight misalignments from the normal incidence position can be detected (Figure 4). The sun alignment precision can be adjusted by increasing or decreasing the distance between the active surface of the LDRs and their small screen.

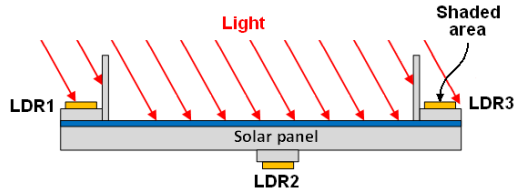


Figure 4. The three *light dependent resistors* (LDR) and their placement on the PV panel.

The electrical circuit for the actuator is divided into the control circuit, and the full-bridge driver (see the schematics in Figures 5 and 6). For simplicity, they are designed to work with a single-ended power supply, which does not have to be stabilized (i.e. could be the actual battery bank that the panel is charging). The final output voltage of the control circuit is half the supply voltage when the panel is properly aligned. This output voltage can be above or below 6 V, which corresponds to moving the panel to the left or to the right as looking from behind in a northern hemisphere location.

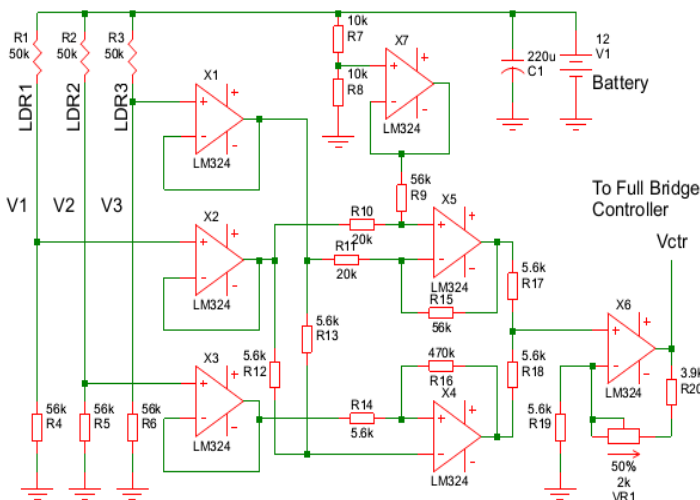


Figure 5. Control circuit schematic.

Each LDR is placed in a voltage divider together with a fixed resistor the value of which is selected based on the dark

and 1 lux resistance of the LDR. Each of the three voltages obtained from the voltage dividers is then buffered with an operational amplifier (op-amp). The op-amps chosen for this design were the LM324 [17] because of their reduced price, good performance and board compactness.

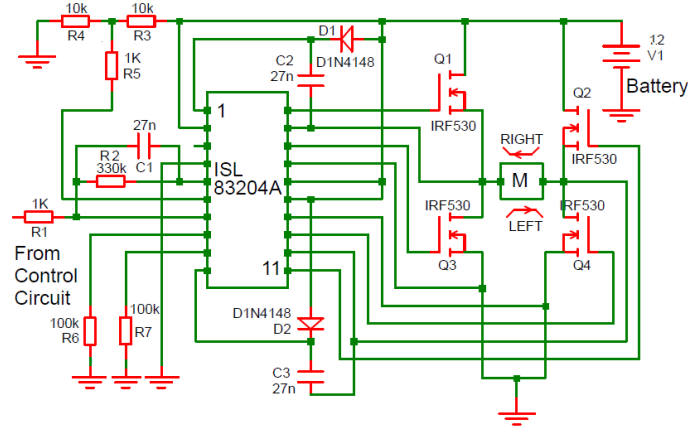


Figure 6. Full-bridge driver circuit diagram.

At any given time during operation, the circuit can be in one of the two modes: (i) normal tracking when the sun is on the front side of the panel or at least voltage $V1$ is significantly higher than $V3$, or (ii) back to sunrise position, when the light falls on the back of the panel. Switching between the two modes is done depending on the output state of op-amp X4 that works as a comparator with hysteresis, comparing voltage $V2$ with $0.5(V1+V3)$ i.e. the average of $V1$ and $V3$. Also, at all times, X5 works as a differential amplifier and its output voltage is in this case equal to $6+2.8(V1-V3)$, which reflects the difference in illumination of the two LDRs on the front of the panel. Since the power supply is single-ended and the LM324 operational amplifiers cannot operate with input voltages close to either *rail* [17], op-amp X7 has been added to provide a local ground for op-amp X5 and to establish a reference for the output voltage. If $V2 > 0.5(V1+V3)$, the output of op-amp X4 will be close to the *positive rail* while the output of op-amp X5 will be negligible because of the small difference between voltages $V1$ and $V3$. Op-amp X6 is used as a summing amplifier in non-inverting configuration, so its output voltage will be $V(X4)+V(X5)$. Because $V(X4)$ will be close to the *positive rail*, $Vctr$ will also be close to the *positive rail*, and so the panel will be rotated to the left. While rotating, at some point voltage $V2$ will become smaller than $0.5(V1+V3)$, and voltage $V(X4)$ will be close to ground value, and voltage $Vctr$ will follow the $(V1-V3)$ difference. At that point, the sun tracker can be said to enter the normal tracking mode. Under balanced conditions, the output voltage will be 6V. Potentiometer VR1 (Figure 5) allows the adjustment of the output voltage to 6V precisely, and is needed because the LM324 operational amplifiers do not provide *rail-to-rail* output capabilities (the output of X4 will never be exactly zero).

The motor driver (Figure 6) is designed as a full-bridge using an INTERSIL ISL83204A [18] integrated circuit in a hysteresis configuration. The full-bridge configuration allows the control of much more powerful actuator motors and can easily be modified to make use of pulse width modulation (PWM) if needed. An added advantage of using the ISL83204A integrated circuit is that only N-channel MOSFET transistors can be used, which increases the reliability and reduces the cost of the circuit. The reference voltage used is 6 V, which corresponds to “best alignment” output level of the control circuit. This voltage should be tapped from the output of op-amp X7. The circuit has internal protection against *shoot-through* by delaying the turn-on point of the low-side drivers, depending on the values of resistors R6 and R7. As configured, this circuit does not have soft-start or soft-stop and does not use pulse width modulation or linear control to run the actuator motor at intermediate speeds. Such options can be added to this stage of the circuit, because the control circuit has been designed as fully analog, and its output voltage varies linearly.

RESULTS AND CONCLUSIONS

A small size prototype of the PV tracker described in the paper has been built and was subjected to a number of mechanical and electrical tests. Short videos of the system in operation are available on YouTube at [19] and [20]. Following these tests the actuator rod had to be supported with a back roller, and the entire panel had to be statically balanced, so that the actuator receives minimum load due to the weight of the panel itself. Additional tests will be performed to monitor the electric power output versus the power consumed by the electrical control system. A comparison between the electric power output of this PV tracker, and an identical no-tracking fixed angle PV panel will also be performed.

REFERENCES

- [1] Regnier, N.J. and Shaeffer, M.R. "Solar Tracking System or the Like" US Pat. 2,913,583.
- [2] Lubitz, W.D. "Effect of Manual Tilt Adjustments on Incident Irradiance on Fixed and Tracking Solar Panels", *Applied Energy*, Vol. 88, 2011, p. 1710-1719.
- [3] Cooke, D. "Single vs. Dual Axis Solar Tracking", *Alternate Energy Magazine*, April-May, 2011.
- [4] Meinel, A.B. and Meinel, M.P. *Applied Solar Energy*, Addison Wesley Publishing Co., 1976.
- [5] Kinematics Manufacturing, Inc., Phoenix, AZ, USA, www.kinematicsmfg.com
- [6] Sedona Solar Technology, Sedona AZ, <http://sedonasolartechnology.com>
- [7] Comsit, M. and Vișa, I. "Design of the linkages type tracking mechanisms of the solar energy conversion systems by using Multi Body Systems Method" Proceedings of the 12th IFToMM World Congress, Besançon, France, June 18-21, 2007.
- [8] Alexandru, C. and Pozna, C. "The Analysis and Optimization in Virtual Environment of the Mechatronic Tracking Systems used for Improving the Photovoltaic Conversion" in *Motion Control*, Casolo, F. (ed.), INTECH, Rijeka, Croatia, 2010, p. 553-580.
- [9] Vișa, I., Diaconescu, D., Săulescu, R., Vătășescu, M. and Burduhos, B., "New Linkage with Linear Actuator for Tracking PV Systems with Large Angular Stroke" *Chinese Journal of Mechanical Engineering*, Vol. 24(5), 2011
- [10] Altuzarra, O., Seras, I., Macho, E. and Aginaga, J. "A Low Energy Consumption Solar Tracker Based in Parallel Kinematics" in *Romansy 19 – Robot Design, Dynamics and Control*, Padois, V., Bidaud P. and Khatib, O. (Edt.), Springer, Vol. 544, 2013, pp 69-76.
- [11] Skoplaki, E. and Palyvos, J.A. "On the temperature dependence of photovoltaic module electrical performance: A review of efficiency/power correlations", *Solar Energy*, Vol. 83, 2009, p. 614–624.
- [12] Press, W.H., Teukolsky, S.A., Vetterling, W.T. and Flannery, B.P. *Numerical Recipes: The Art of Scientific Computing*, 3rd ed., Cambridge University Press, 2007.
- [13] Uicker, J.J., Pennock, G.R. and Shigley, J.E. *Theory of Machines and Mechanisms*, Oxford University Press, 2010.
- [14] Lánčzos, C. *The Variational Principles of Mechanics*, 4th ed., University of Toronto Press, 1970.
- [15] Simionescu, P.A. and Mehrubeoglu, M. "New Concepts on Two-Dimensional Data Visualization with Applications in Engineering Analysis and Design" *Journal of Computing and Information Science in Engineering*, Vol. 12(2), 024501, 2012, 10 p.
- [16] Simionescu, P.A., *Computer Aided Graphing and Simulation Tools for AutoCAD Users*, CRC Press, 2014.
- [17] LM124-N/LM224-N/LM324-N/LM2902-N "Low Power Quad Operational Amplifiers Datasheet", Texas Instruments, 2004.
- [18] ISL83204A Data Sheet, Intersil Americas Inc., 2007.
- [19] <http://www.youtube.com/watch?v=tj29GmWByVk>
- [20] http://www.youtube.com/watch?v=0aw8y_fs3Ik